Nanoscale

Direct Observation of Magnetic Ordering induced via Systematic Lattice Disorder in Artificial Rhombus Spin Ices

Journal:	*Nanoscale*
Manuscript ID	NR-ART-03-2023-001012.R1
Article Type:	Paper
Date Submitted by the Author:	22-May-2023
Complete List of Authors:	Cote, Timothy; Northwestern University, Materials Science & Engineering; Argonne National Laboratory, Materials Science Division Petford-Long, Amanda K.; Argonne National Laboratory, Materials Science Division; Northwestern University Phatak, Charudatta; Argonne National Laboratory, Materials Science Division; Northwestern University, Department of Materials Science and Engineering

ARTICLE

Direct Observation of Magnetic Ordering induced via Systematic Lattice Disorder in Artificial Rhombus Spin Ices

Timothy Cote,*[a, b] Amanda K. Petford-Long [a, b] and Charudatta Phatak [a, b]

Received 00th January 20xx,
Accepted 00th January 20xx

DOI: 10.1039/x0xx00000x

It is critical to understand the effect of lattice geometry on the order parameter of a condensed matter system, as it controls phase transitions in such systems. Artificial spin ices (ASIs) are two-dimensional lattices of Ising-like nanomagnets that provide an opportunity to explore such phenomena by lithographically controlling the lattice geometry to observe its influence on magnetic ordering and frustration effects. Here we report a systematic approach to studying the effects of disorder in rhombus ASIs generated from combinations of five vertex motifs. We investigate four geometries characterized by a geometric order parameter, with symmetries ranging from periodic to quasiperiodic to random. Lorentz transmission electron microscopy data indicates magnetic domain behavior depends on chains of strongly-coupled islands in the periodic and sixfold-twinned lattices, while the behavior of the disordered lattice is dominated by vertex motifs with large configurational degeneracy. Utilizing micromagnetic simulations, a quantitative analysis of the lattice energetics showed that the experimental rotationally-demagnetized state of the disordered ASI was closer in energy to the idealized ground state compared to other periodic and twinned ASIs. Our work provides a unique pathway for using degeneracy, magnetic frustration, and order to control the magnetization behavior of designer disordered systems.

Introduction

It is a truth universally acknowledged, that a geometrically constrained lattice of islands in possession of magnetic moments, must be in want of magnetic frustration. For an artificial spin ice (ASI), this gives rise to emergent phenomena, most notably magnetic monopoles, which had long been predicted[1,2] and are now a tunable aspect of ASI behavior.[3,4] Along with novel phases such as magnetic-charge ordered phases, smectic phases, and spin liquid phases,[5–10] ASIs have spawned rich avenues for potential novel computation with magnetic architectures.[11,12] One desirable trait of ASIs is their geometric tunability in 2-D and in 3-D.[3,5,13–21] While periodic ASIs have been extensively studied, the introduction of disordered and aperiodic geometries garnered interest due to the complex interactions that can lead to arrested spin-glass dynamics[16] and dendritic magnetization reversal behavior.[17,22–24] One key aspect governing the collective magnetization behavior in these lattices are the motifs located at the vertices in which nanomagnets meet. The mixed coordination (i.e., different number of nanomagnets) of the vertex motifs leads to 'vertex frustration', which prevents all motifs from occupying their lowest energy configuration.[8] Controlling this additional level of frustration by controlling the ASI lattice geometry allows for the exploration of exotic collective behavior such as reduced dimensionality in 2D ASIs and extended magnetic frustration.[13,25] Recent efforts which investigated the dynamics of long-range disordered ASIs[26,27] have shown promise for the creation of rich magnonic systems. In addition, understanding the intricate interactions in progressively complex geometries like the Cayley tree[28] and Hopfield network[16] ASIs have successfully led to artificial spin-glass behavior.

These remarkable aspects of ASI behavior can advance the development of low power computation and compute-in-memory neural-network devices.[29] However, a systematic approach to understanding the effect of lattice disorder on the resulting magnetic frustration is still lacking. A systematic approach to creating ASIs with rotational and translational randomization[30] has shown that critical behavior is disorder dependent, but a lack of *local* understanding of the nanomagnet interactions limits finer control of the magnetic behavior. Another systematic yet simple approach to introduce disorder is to remove nanomagnets from a periodic lattice through decimation. The number of distinct vertex motifs in a decimated lattice is much lower than in a completely randomized ASI, which permits a finer understanding of local behavior. Decimated square lattices such as the periodic tetris,[13] Shakti,[14] and Santa Fe[15] lattices have enabled the exploration of the

[a] *Materials Science Division, Argonne National Laboratory, Lemont, IL, 60439, USA.*
[b] *Department of Materials Science and Engineering, Northwestern University, Evanston, Illinois 60208, USA*
Electronic Supplementary Information (ESI) available: See DOI: 10.1039/x0xx00000x

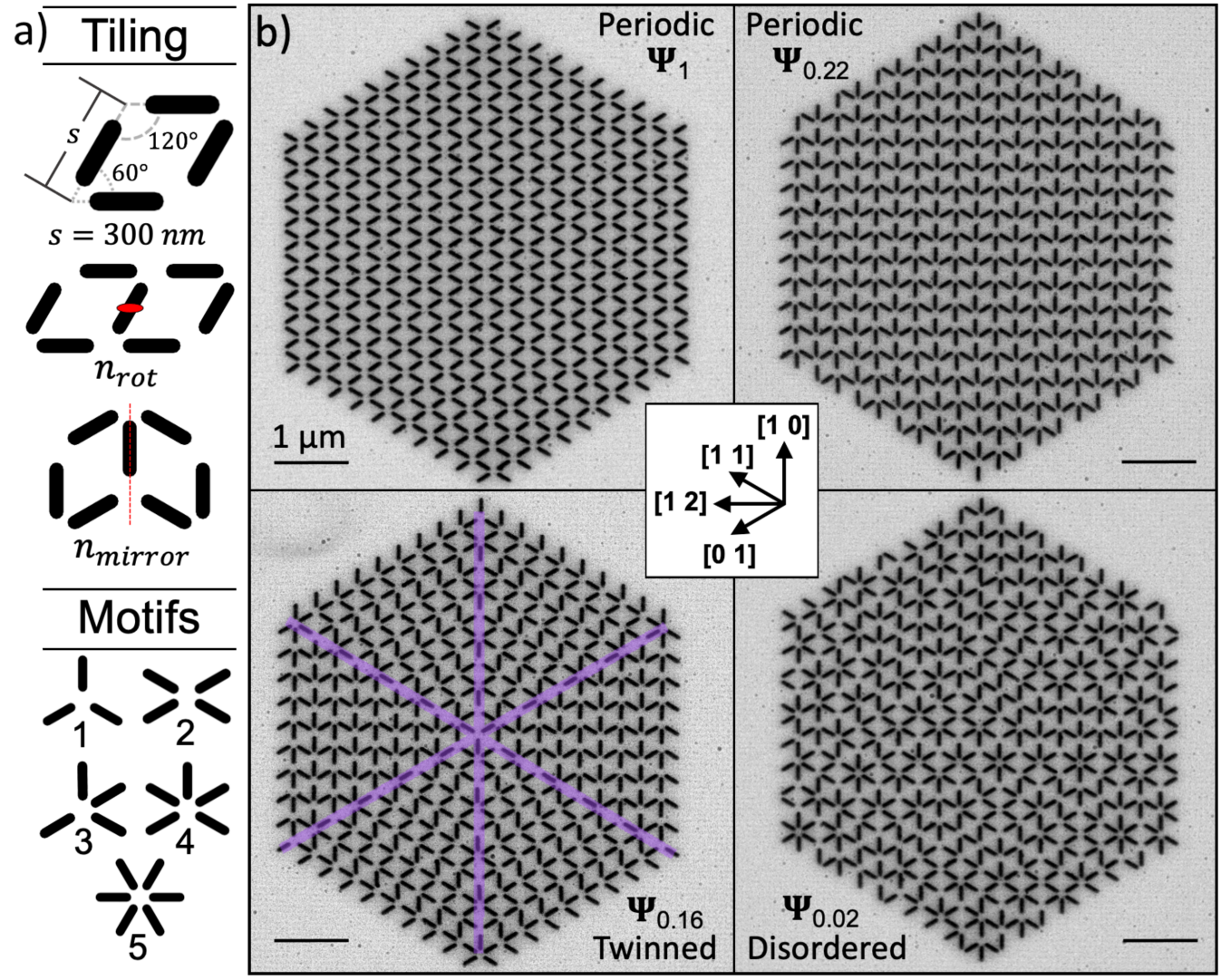

Figure 1. (**a**) Sub-units of the RASIs: 60°-120° tile with vertex-vertex distance s; tiles that share an island have rotational, n_{rot}, or mirror, n_{mirror}, symmetry; five distinct motifs that occur in the different RASIs. (**b**) Bright-field TEM images of the periodic, sixfold-twinned, and disordered RASIs with Ψ_1, $\Psi_{0.22}$, $\Psi_{0.16}$, and $\Psi_{0.02}$, respectively. Hexagonal lattice directions (inset in **b**) are used to describe anisotropic behavior.

effects of vertex frustration on magnetic behavior, with theoretical work indicating the behavior of a randomly-decimated square ASI lattice can give rise to a low temperature glassy phase.[31]

To further understand the role of geometric complexity and frustration on magnetic ordering, we have studied rhombus artificial spin ices (RASIs),[32] with different geometries and lattice symmetries, all based on a single rhombus tile. Lorentz transmission electron microscopy (LTEM) was used to characterize the magnetic induction of the ASIs, allowing us to explore how the degree of disorder alters the magnetic domain behavior and to provide insights into the driving forces for emergent magnetic ordering in complex spin systems.

Results & discussion

Results

In order to systematically vary the lattice geometry and long-range order, we designed the RASIs utilizing a rhombus tile as shown in Figure 1a. Two adjacent rhombus tiles share a single magnetic island and are related by one of two symmetry operations, namely rotation or a mirror-plane. This limits the RASI lattice to contain five possible vertex motif types (Fig. 1a), with islands surrounding the motif's central vertex. Motifs are combined and arranged on the lattice to create RASIs with different global symmetries. Each RASI was fabricated from Co nanomagnets using direct electron-beam-induced deposition with seed and capping layers of C to prevent oxidation. An additional Al capping layer was deposited via electron-beam evaporation to further prolong oxidation resistance. Each lattice was designed to have between 570 and 582 stadium-shaped islands with lateral dimensions of 200 nm × 50 nm and a thickness of 10 nm. The vertex-vertex separation, s, was 300 nm with islands centered between vertices. Additional fabrication details are given in the Experimental section.

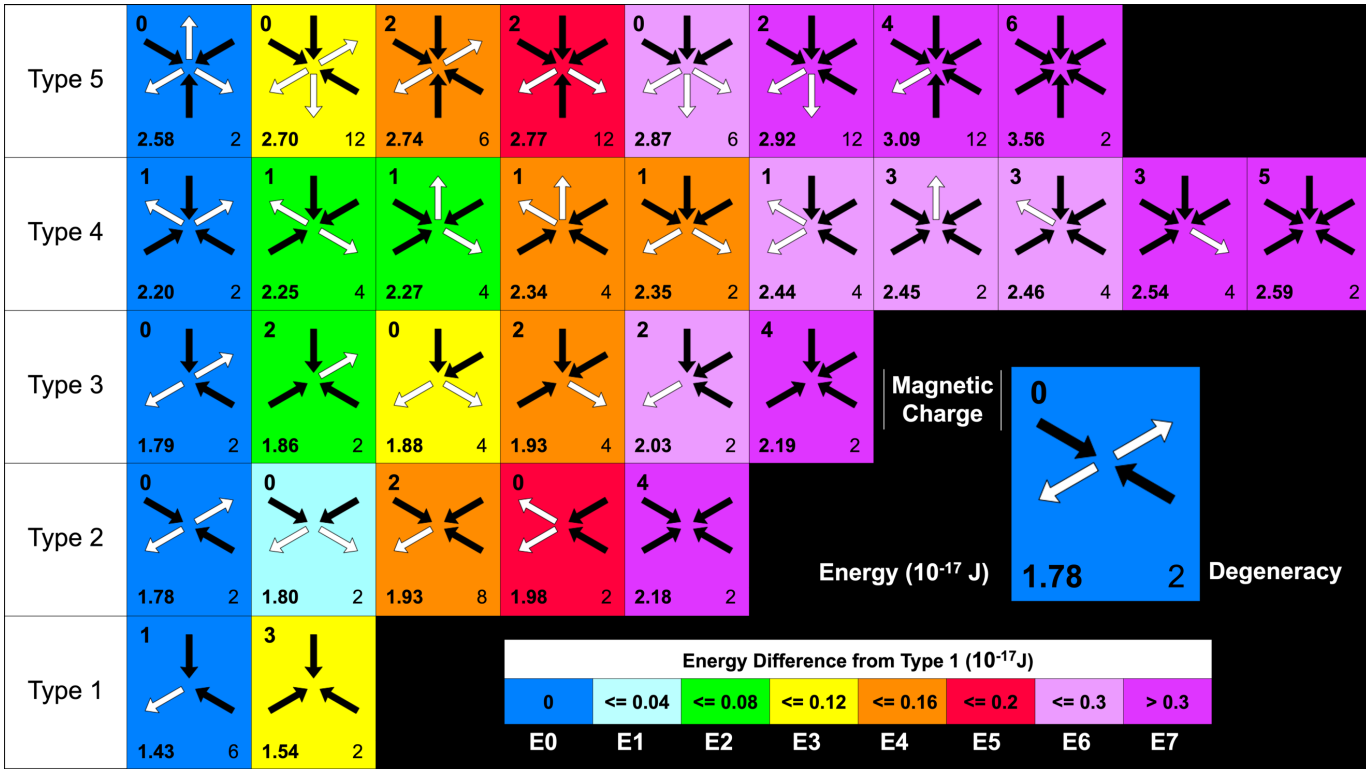

Figure 2. Table showing the energy, degeneracy, and absolute magnetic charge of each magnetization configuration for the RASI motifs. Black and white arrows distinguish magnetization directed toward or away from a motif's vertex. Energy increases from left to right for a given motif, and from bottom to top for different motifs. The energy of the magnetic configurations is binned and color-coded by the absolute difference in energy relative to the E0 configuration (see inset).

To quantify and differentiate the RASIs, a geometric order parameter was used to classify each lattice,[33]

$$\Psi = \frac{0.608n_{rot} - 0.392n_{mirror}}{0.608n_{rot} + 0.392n_{mirror}}$$

where n_{rot} is the population of islands with 1st and 2nd nearest neighbors with 2-fold rotational symmetry, and n_{mirror} is the population of nearest neighbors with mirror symmetry, as shown in Figure 1a. Lattices have characteristic Ψ values in the range $-1 \le \Psi \le 1$, and we classify each ASI by a shorthand notation so that Ψ_1 refers to the lattice for which $\Psi = 1$. If all islands populate n_{rot}, the lattice will be of the Ψ_1 type. Conversely, if all islands belong to the n_{mirror} classification, the lattice is of the Ψ_{-1} type. A random lattice is defined as Ψ_0 and we limited our study to lattices with $\Psi > 0$. We investigated four different RASI lattices of Figure 1b-e: two periodic RASI geometries (Ψ_1 and $\Psi_{0.22}$), a sixfold-twinned lattice ($\Psi_{0.16}$), and a disordered geometry ($\Psi_{0.02}$). The Ψ_1, $\Psi_{0.22}$, and $\Psi_{0.16}$ RASIs show global 2-fold mirror, mirror, and 3-fold mirror symmetry respectively. The $\Psi_{0.02}$ RASI lacks any long-range order. It should be noted that the Ψ_1 and $\Psi_{0.22}$ lattices have the same vertex coordination as a square ASI, although a square ASI has 4-fold rotational mirror symmetry. In terms of the vertex motifs, the Ψ_1 RASI contains only Type 2 motifs and $\Psi_{0.22}$ contains only Type 3 motifs. For $\Psi_{0.16}$, three motifs (Types 1, 3, and 4) of mixed coordination are present: large regions containing the Type 3 motif (identical to the lattice in the $\Psi_{0.22}$ RASI) are separated by domain boundaries formed from alternating Type 1 and Type 4 motifs (Fig. 1d). Lastly, the disordered $\Psi_{0.02}$ lattice contains all five motifs in a random arrangement across the lattice. The two-dimensional hexagonal lattice directions shown in Figure 1 are used to describe the domain behavior of the ASIs, with the [1 0] direction aligned to the vertical image axis.

We explore the magnetization behavior of the RASIs by analyzing the energetics of the magnetic configurations in the vertex motifs for two states: the remnant state after rotational demagnetization and a simulated ground state. By quantifying the presence of local motif excitations in the demagnetized state, we can understand the magnetic domain behavior of the RASIs and determine the efficacy of rotational demagnetization as a means of approaching the ground state of each lattice. We performed micromagnetic simulations using MuMax3[34] software to determine the energy of all unique magnetic configurations for each motif and generate a table (color-coded by energy), shown in Figure 2. The enlarged motif diagram shows the lowest energy E0 configuration for the Type 2 motif with the absolute magnetic charge, absolute energy, and configurational degeneracy inset. This information is shown for each magnetic configuration. Due to the size and shape of the islands, the magnetization is Ising in nature and directed toward or away from the motif's vertex. Configurations with higher energy (E1 or above) are considered excitations above the E0 configuration. The configurations were categorized into color-coded energy states according to the absolute energy difference of the configuration from the E0 state, as shown in the inset Table for all states labeled E0—E7. The lowest energy configuration for each motif obeys the Berner-Fowler spin ice rules,[35] minimizing the overall magnetostatic energy by having

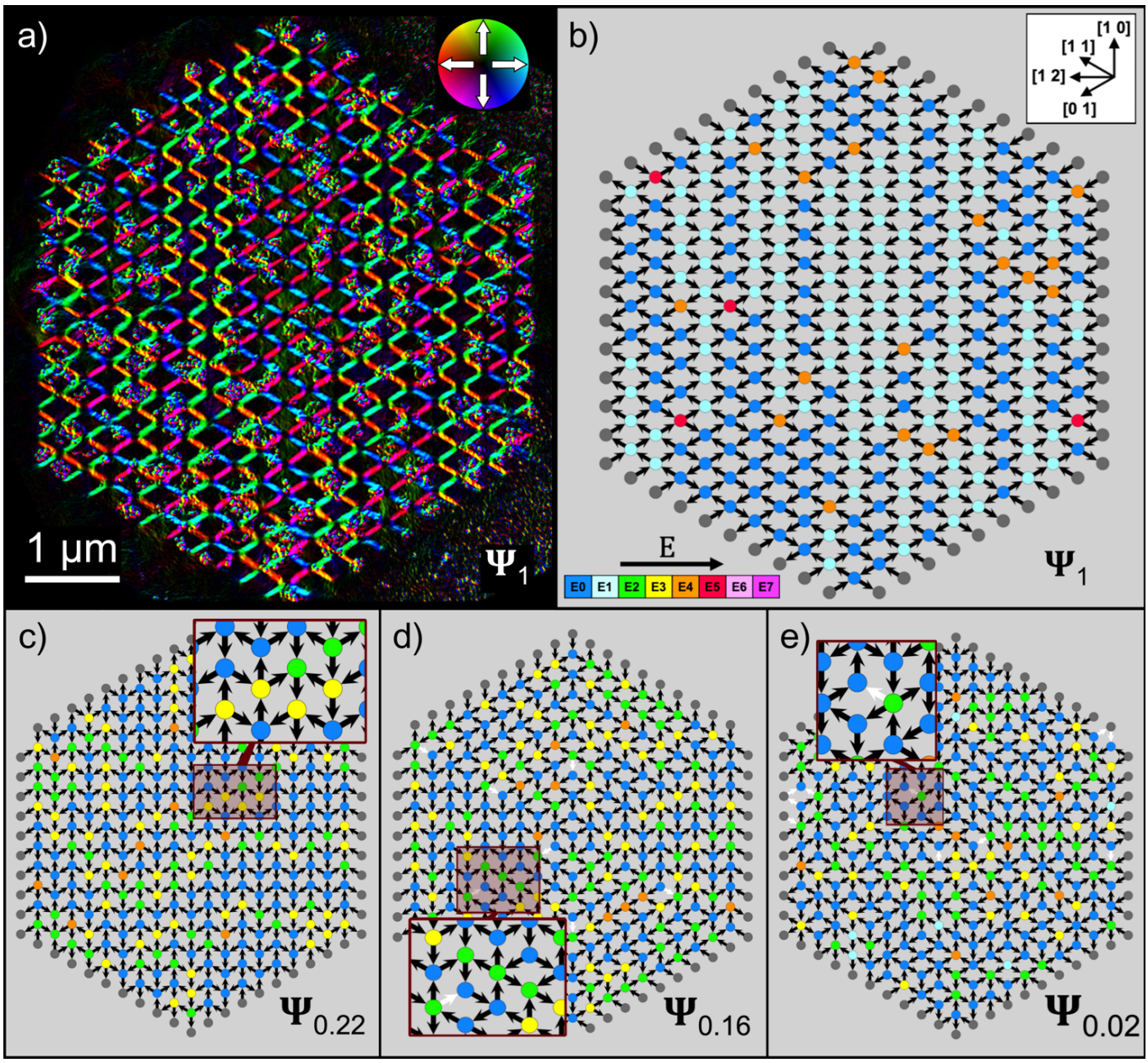

Figure 3. Magnetization configurations of the demagnetized state. (**a**) LTEM reconstructed magnetic induction map for the Ψ_1 RASI. The magnetization direction of the islands corresponds to the inset color-wheel. (**b–e**) Directed graphs showing the energy states for RASIs with Ψ_1, $\Psi_{0.22}$, $\Psi_{0.16}$, and $\Psi_{0.02}$, constructed from the experimental LTEM data (note: (**a**) maps to (**b**)). Directed arrows represent the magnetization of islands; nodes correspond to motifs and are colored according to their configurational energy. White arrows represent degenerate spins with no energetic preference for magnetization direction.

the magnetization in adjacent islands alternating in direction toward or away from the vertex. As the coordination of a motif increases, both the number of unique configurations and the motif energies increase as well. However, higher symmetry reduces the number of distinct configurations and leads to higher degeneracy as seen for motif Types 1, 2, and 5.

We performed LTEM experiments to explore the magnetic domains present in each RASI. Experimental images of the remnant state were acquired following a rotational demagnetization protocol designed to minimize the net magnetization. In-plane magnetic induction maps were reconstructed from through-focal series of LTEM images utilizing phase-retrieval methods.[22,36] Figure 3a shows the reconstructed color magnetic induction map for the Ψ_1 periodic RASI in the rotationally-demagnetized state. The direction of magnetization corresponds to the inset color-wheel. The high spatial resolution of LTEM allowed us to confirm the single domain behavior for each island. To analyze how the motif energies are distributed across each RASI, directed graphs (Fig. 3b–e), in which the colored nodes correspond to the vertices of the motifs, were created from the experimental magnetic induction maps for the demagnetized states of the Ψ_1, $\Psi_{0.22}$, $\Psi_{0.16}$, and $\Psi_{0.02}$ lattices. Nodes are color-coded according to the motif configurational energy table shown in Figure 2. The directed arrows correspond to the magnetization directions of the islands. White arrows (referred to here as 'degenerate

spins') indicate islands that have no preference in magnetization direction, as each direction produces an energetically equivalent configuration.

For Ψ_1, two predominant types of order are present in the demagnetized state with most motifs being either in the lowest energy E0 state (dark blue) or in the 1st excited E1 state (cyan) as seen in Figure 3b. We observe chains of islands with net magnetic moment oriented along the [1 0] direction. These chains terminate either at lattice edges or at higher energy motifs in the E4 excited state with remnant magnetic charge or the E5 excited states with no magnetic charge. Although the vertex separation is constant, the spacing between the ends of neighboring islands is narrower along the [1 0] direction than along the [1 2] direction, leading to the anisotropic domain behavior.

$\Psi_{0.22}$ contains many small magnetic domains of Type 3 motifs that are in the lowest-energy E0 state. These domains are separated by domain walls consisting of motifs in the E2, E3, and E4 states, as seen in Figure 3c. For $\Psi_{0.22}$, domain walls predominantly order along the symmetrically equivalent [0 1] and [1 1] directions but can also order along the [1 0] direction. If two motifs share an island and both occupy the E2 state, the motifs will have opposite magnetic charge if the shared island points along the [0 1] or [1 1] directions. If instead the motifs in the E2 state order along the [1 0] direction, each motif will have magnetic charge of the same sign. Motifs in the E3 state (yellow) also order along the [1 1], [0 1], and [1 0] directions. Motifs in the E4 excited state (orange) have net magnetization along [1 2] and are randomly distributed throughout the lattice. Motifs in excited states are located either in domain walls or at the edge of the lattice.

The $\Psi_{0.16}$ RASI of Figure 3d is created by joining three domains of the $\Psi_{0.22}$ lattice in different orientations to create a RASI with 3-fold rotational mirror symmetry. It is therefore expected to display similar behavior to the demagnetized state of $\Psi_{0.22}$ within the domains comprised of the Type 3 motifs, as is indeed the case. A new feature of the $\Psi_{0.16}$ lattice is the appearance of degenerate spins between Type 1–Type 4 motif pairs along the structural domain boundaries. In general, motifs along the domain boundaries are in their lower energy configurations with 100% of the Type 1 motifs populating the E0 state. While the Type 4 motifs do not fully occupy E0, no motifs have energies higher than the E2 state.

For the demagnetized state of the disordered $\Psi_{0.02}$ lattice seen in Figure 3e, there are some similarities in motif behavior to the ordered lattices. The Type 1 motifs predominantly occupy the E0 energy state as seen for $\Psi_{0.16}$. Type 2 motifs behave like those in the Ψ_1 RASI, residing in one of the two lowest energy states. Additionally, connected Type 3 motifs show similar ordering to that seen in the $\Psi_{0.22}$ and $\Psi_{0.16}$ lattices. One difference is the behavior of the Type 4 motifs, which occupy higher energy states in $\Psi_{0.02}$ compared to $\Psi_{0.16}$. Slight magnetic charge ordering also occurs locally between neighboring motifs. Energetically unfavorable motif configurations with higher net

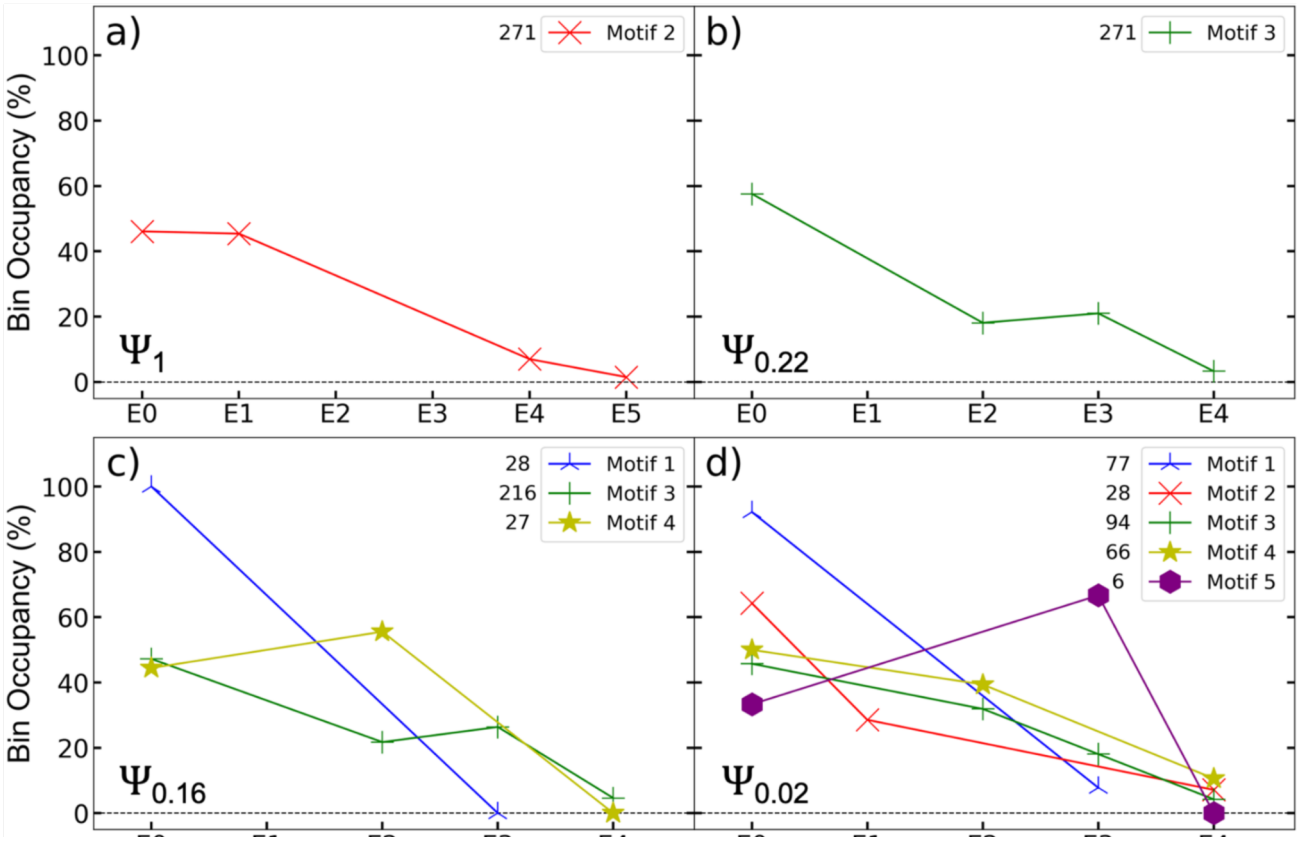

Figure 4. (**a–d**) Motif energy state occupancy of the demagnetized state for each RASI, with the population of each motif included. As expected, the population of motifs in higher energy states decreases with increasing energy. However, this trend breaks for Motif 3 in $\Psi_{0.22}$ and $\Psi_{0.16}$, for Motif 4 in $\Psi_{0.16}$, and for Motif 5 in $\Psi_{0.02}$. No error bars are present, as we could directly identify and count the motif configurations due to the high resolution of our LTEM images.

magnetization are not observed. There are six Type 5 vertex motifs in this RASI, four of which occupy the E3 state and two of which occupy the E0 state.

Statistical analysis of the demagnetized state for each RASI is shown in Figure 4a-d, with plots showing the energy state occupancy of the motifs for each RASI. For Ψ_1 (Fig. 4a), the motifs predominantly occupy the E0 and E1 energy states, with populations of 46.1% and 45.4% respectively. Near equal populations of the E0 and E1 states result from the small difference in energy between these configurations. For $\Psi_{0.22}$ (Fig. 4b), which contains only Type 3 motifs, the E0 state has the largest population as expected. In terms of the excited states, the E3 state has a higher occupancy (21.0%) than the lower energy E2 state (18.1%). The same trend is seen in $\Psi_{0.16}$ (Fig. 4c) where there is higher occupancy of the E3 state compared to E2 (26.4% to 21.8%). Type 1 motifs, which occur only at the structural domain boundaries in $\Psi_{0.16}$, all occupy their lowest energy E0 state. Type 4 motifs fill the E0 and the E2 states with occupations of 44.4% and 56.6%, respectively.

Finally, Figure 4d shows the motif behavior for the demagnetized state of the disordered $\Psi_{0.02}$ lattice. Type 1 motifs again have the largest E0 population. However, the Type 2 motif shows a different behavior from that seen for Ψ_1. Although nearly all Type 2 motifs occupy the E0 and E1 states, the E0 population is significantly larger than that of the E1 state (64.3% versus 28.6%), compared to the same populations seen for Ψ_1 (46.1% versus 45.4%, Fig. 4a). Another difference in behavior is that of the Type 3 motifs. Compared to $\Psi_{0.22}$ and $\Psi_{0.16}$, the E2 state has a higher occupation than the E3 state with filling of 31.9% versus 18.1% respectively. For the Type 4 motif, state occupation consistently decreases with increasing energy. $\Psi_{0.02}$ is the only RASI with Type 5 motifs and although there are only a few of them in the lattice, they only occupy the two lowest permissible energy states (E0 and E3) with the excited state having higher occupancy.

Theoretical ground states were calculated for each RASI using the motif energy model and were compared to the experimental rotationally-demagnetized data. By simulating the predicted ground state of each RASI, we can make a quantitative and qualitative analysis of the effectiveness of rotational demagnetization at lowering the lattice energy. Previous work has shown that rotational demagnetization is not as effective as thermal annealing for lowering the energy of periodic lattices such as a square ASI[37,38] but was effective for a

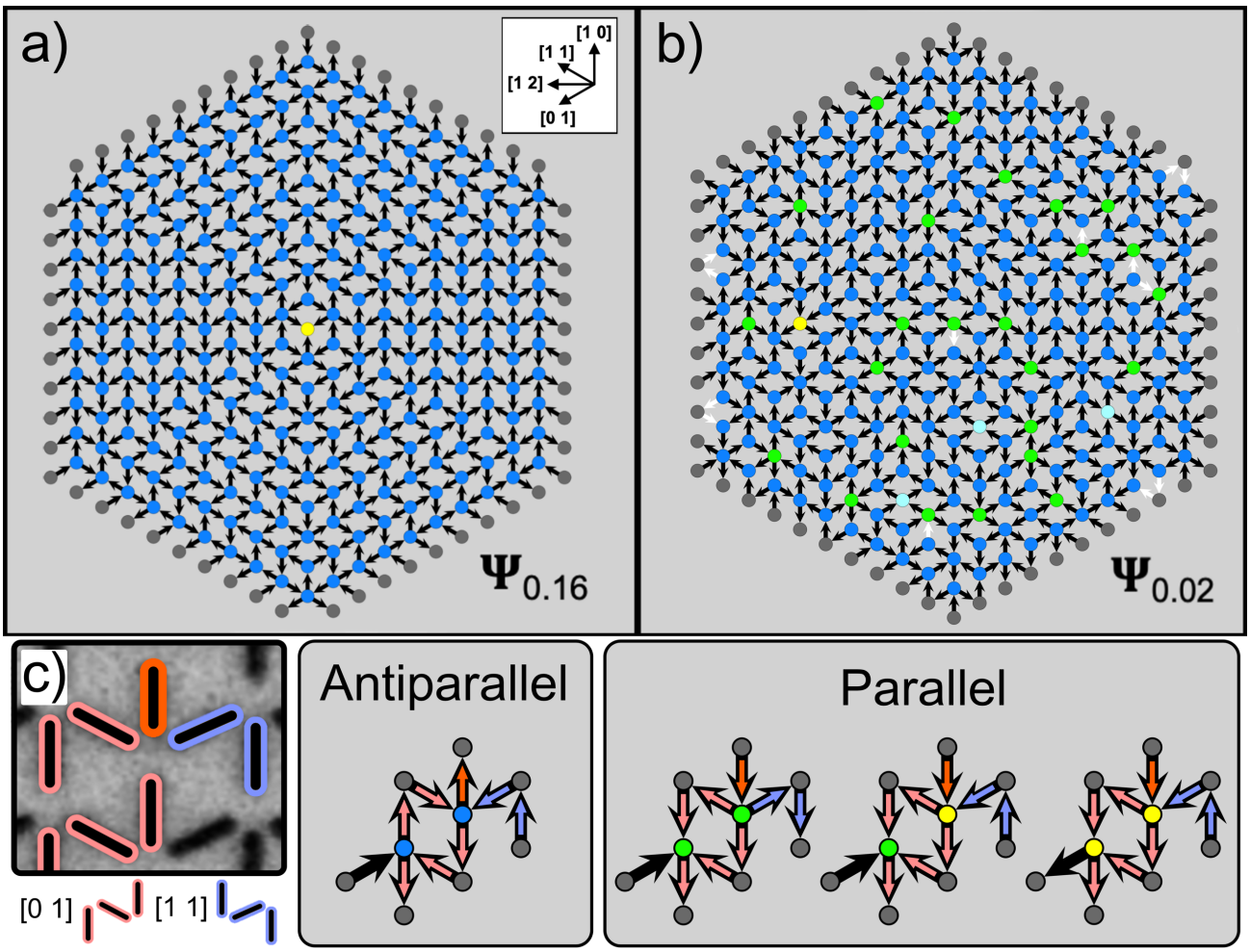

Figure 5. Idealized ground state for (**a**) $\Psi_{0.16}$ and (**b**) $\Psi_{0.02}$ RASI. Vertex frustration results in higher energy motif configurations. Multiple degenerate spins appear randomly throughout the $\Psi_{0.02}$ RASI. Bright field TEM image of the $\Psi_{0.22}$ lattice (**c, left**) with examples of islands that are part of three-island chains outlined. Chains oriented in the same direction can form antiparallel (**c, middle**) or parallel (**c, right**) spin orderings. [0 1] and [1 1] chains share an island which is frustrated if it belongs to an E3 motif state.

quasicrystalline ASI.[36] The ground-state ordering for the Ψ_1 and $\Psi_{0.22}$ RASIs has the same ordering of a square ASI, with all motifs occupying the E0 state. For $\Psi_{0.16}$, shown in Figure 5a, the ground-state ordering also has all motifs occupying the E0 state, except for one Type 1 motif situated on the 3-fold rotational axis, which is in the E3 excited state. For these three ASIs, the ground state is two-fold degenerate due to time-reversal symmetry, which requires flipping all spins to access one state from the other.

Unsurprisingly, the increased frustration within the disordered $\Psi_{0.02}$ RASI lattice increases the complexity of the ground state. As is the same for the periodic and sixfold-twinned RASIs, the majority of spins in $\Psi_{0.02}$ participate in a globally two-fold degenerate magnetic ordering where the two states are related by reversing all participating spins. These spins are indicated by the black arrows in Figure 5b. Setting the magnetization direction for any individual spin (within this larger set of participating spins) will dictate the preferred magnetization direction for all other spins in the set. However, there are also a few islands shared between Type 1 and Type 4 motif pairs which act as degenerate spins (shown as white arrows), such that reversing their direction does not change the local energy or the surrounding magnetic configuration. Due to vertex frustration, several motifs are constrained to occupy higher energy states that cannot be eliminated without introducing motif configurations that would increase the global energy. For the disordered RASI that we have explored here, this results in some of the Type 2 motifs occupying the E1 state, a small population of Type 3 motifs occupying E2 and E3 states, and some Type 4 motifs occupying the two different magnetic configurations in the E2 state.

A quantitative analysis of the difference in normalized net magnetization, $\Delta|M|$, between the rotationally-demagnetized state and the simulated ground state was carried out for each RASI. Each island was assigned a magnetization magnitude $|\boldsymbol{m}| = 1$ and the total normalized net magnetization is given by $|M| = M_{sat}^{-1}\sqrt{(\sum m_x)^2 + (\sum m_y)^2}$ where m_x and m_y are the components of magnetization of an island. To relate the magnetization behavior between lattices, we normalize $|M|$ by the saturation magnetization M_{sat} prior to calculating the normalized difference in net magnetization between states, $\Delta|M|$. The standard error of $|M|$ is calculated from the standard deviation of the distribution of nanoisland magnetic moments. $|M|$ is 0 for the ground state of the Ψ_1 and $\Psi_{0.16}$ lattices. $|M| > 0$ but small for the ground state of $\Psi_{0.22}$ because of uncompensated spins at the edge of the lattice. For the disordered RASI ($\Psi_{0.02}$), the ground state has the largest non-zero net-magnetization. A comparison of $\Delta|M|$ for the different lattices is shown in Table 1. We observed the lowest value of $\Delta|M| = 2.60 \times 10^{-2}$ for the Ψ_1 lattice, with the cumulative net magnetization of the separate ferromagnetic domains with magnetization along the positive and negative [1 0] directions cancelling. The $\Psi_{0.22}$ and $\Psi_{0.16}$ RASI have corresponding $\Delta|M| = 5.76 \times 10^{-2}$ and 3.70×10^{-2}. In these lattices, the E3 energy state is the largest contributor to the net magnetization, and the increased 3-fold lattice symmetry of $\Psi_{0.16}$ lowers the total net magnetization relative to the "single domain" $\Psi_{0.22}$ lattice. For the disordered RASI ($\Psi_{0.02}$), $\Delta|M|$ has the largest value of 7.15×10^{-2}, as multiple motifs like Motif 1 and Motif 4 occupy low-energy excited states that have larger net magnetization and are not compensated across the lattice.

Table 1. The normalized net magnetization difference and normalized energy difference between the demagnetized state and simulated ground state for each RASI.

Ψ	$\Delta\|M\| \times 10^2$	ΔE^*
1	2.60 ± 1.31	13.1 ± 0.8
0.22	5.76 ± 1.07	19.3 ± 0.7
0.16	3.70 ± 0.83	20.6 ± 0.7
0.02	7.15 ± 0.82	13.8 ± 0.7

Discussion

Qualitative and quantitative differences in the magnetic domain behavior and energy landscape were investigated for the four different rhombus ASI lattices. By altering the populations of different vertex motifs in the four RASIs, we varied the long-range periodicity, giving rise to different domain behavior. We calculated the total energy of the rotationally-demagnetized states and the ground states by summing the energy of the individual vertex motif magnetic configurations. The self-energy of each island is double counted in each case as they are shared by two motifs. For consistency, we double-counted the single islands at the lattice edges. This method does not give the explicit energy of any particular state, but it allows us to make observations about the relative difference in energy (ΔE) between the ground state and the rotationally-demagnetized state. We normalize the energy difference ΔE by the island self-energy, E_{island} (4.09×10^{-18} J), to give the unitless, normalized energy difference $|\Delta E^*| = |\Delta E| E_{island}^{-1}$. This allows us to quantify the total energy difference between the demagnetized and ground state configurations of the RASI lattices. The error in ΔE^* is given by the standard error of the standard deviation of the distribution of individual motif energies. A comparison of ΔE^* for the different lattices is shown in Table 1. The demagnetized states of Ψ_1 and $\Psi_{0.02}$ are closest in energy to the ground state, with ΔE^* of 13.1 and 13.8, respectively. Compared to the ΔE^* values for Ψ_1 and $\Psi_{0.02}$, ΔE^* is greater for $\Psi_{0.22}$ and $\Psi_{0.16}$ RASI with corresponding values of 19.3 and 20.6.

For the Ψ_1 RASI, formed only from Type 2 motifs, we observed the formation of ferromagnetic stripe domains aligned along the preferred [1 0] direction in the demagnetized state. Domains of motifs in their antiferromagnetic ground state were present as well, with the same [1 0] alignment. These two different domains are a consequence of the inherent anisotropy of the Type 2 motifs. Consider the Type 2 motif orientations in the RASI shown in Fig. 1b: the separation between nearest neighboring islands that are oriented such that their net magnetic moment is along the [1 0] direction is narrower than between neighboring islands with net moment along [1 2], and therefore the coupling is stronger. This results in neighboring islands with net moment along [1 0] favoring a head-to-tail spin alignment, which is the case for the low-energy E0 and E1 Type 2 motif configurations. When all Type 2 motifs share the same orientation as in Ψ_1, neighboring strongly-coupled islands form

a strongly-coupled island chain along the [1 0] direction that extends across the entire lattice and also preferentially shows the head-to-tail spin ordering. Collective ordering of island chains in the lattice results in the anisotropic formation of low-energy magnetic domains consisting of E0 and E1 configurations, which lower the overall global energy of the lattice. Island chains show behavior similar to the so-called "Dirac strings"[1] in square ASIs,[39] which are chains of islands with reversed spins, terminated by monopole pairs. In our case, the islands chains behave more like the observable flux tube of Nambu monopole pairs.[40] However, there is a slight difference in the case of the demagnetized state of the Ψ_1 lattice, where two excitations are observed: a low-energy excitation with remnant magnetic charge and a high-energy, zero-charged, strongly-polarized excitation. For the $\Psi_{0.22}$ and $\Psi_{0.16}$ lattices, the magnetization behavior is governed by the Type 3 motifs, which prefer to occupy the E0 state. As a result of the same strong coupling that gives rise to the island chains of the Ψ_1 RASI, the Motif 3 vertices in $\Psi_{0.22}$ and $\Psi_{0.16}$ form shorter "chains" consisting of a maximum of three islands. Examples of this island chain formation are shown in the LTEM image of the $\Psi_{0.22}$ RASI in Figure 5c. Island chains occur along the [0 1] (red) and [1 1] (blue) directions, and [0 1] and [1 1] chains mutually share an island (orange). Chain colors have no relation to the motif energies. Island ends within a chain are closely spaced, which increases the island-island coupling strength and causes the islands to prefer head-to-tail spin alignment. Figure 5c shows four orderings of part of a Type 3 motif arrangement in $\Psi_{0.22}$ and $\Psi_{0.16}$ which contains two [0 1] chains and a [1 1] chain. Each of the four states has head-to-tail ordering of spins within each [0 1] chain, but the upper and lower chains have either antiparallel or parallel ordering relative to each other. The antiparallel ordering with two E0 motif states is energetically favorable. Three higher energy parallel spin orderings are possible: one ordering with two E2 vertex motif states, another with two E3 states, and an ordering with one E2 state and one E3 state. As the spacing between island ends determines the strength of the magnetic interactions, the interactions between islands of the upper and lower chains are weaker than the interactions between islands within a chain. Thus, a new frustration emerges; energetics favors antiparallel chains with motifs occupying the E0 state, but there are more opportunities for chains to enter a parallel ordering with a slight energy penalty. In addition to chains with the same lattice orientation having parallel or antiparallel magnetic ordering, another source of frustration stems from chains with different orientations that share an island. The spin direction of a mutually shared island can be frustrated when the magnetic ordering of both chains cannot have spins ordered head-to-tail. Such is the case in the arrangement of Figure 5c containing two E3 motif states where the [0 1] chains have head-to-tail spin ordering but the [1 1] chain does not. The blue middle spin of the [1 1] chain has head-to-head alignment with the orange spin that is shared with a [0 1] chain. Removing the E3 motif state requires multiple spin reversals to transition to a lower-energy configuration where the [1 1] chain has head-to-tail alignment of spins. In essence, once an E3 state populates a vertex motif, it is difficult for an E3 state to be removed from the lattice. Cumulatively, the multifaceted frustration of island chains in the $\Psi_{0.22}$ and $\Psi_{0.16}$ RASIs results in larger populations of motif excitations that impede the formation of low-energy domains and results in the ordering of higher energy domain walls along the lattice directions equivalent to [0 1] and [1 1].

The $\Psi_{0.16}$ and $\Psi_{0.02}$ lattices contain odd-coordinated Type 1 and Type 4 motifs that introduce geometric disorder into the RASIs. However, increasing the geometric disorder did not immediately result in magnetic disorder between islands. Due to the degeneracy of the Type 1 ground state configuration, other motifs that are connected to a Type 1 motif can transition to an antiferromagnetic E0 configuration without raising the Type 1 motif energy. Thus, while Type 1 and Type 4 motifs create unavoidable vertex frustration, a large population of Type 1 motifs limits its effect to create magnetic disorder. Similarly, an increased prevalence of Type 1 motifs enhances the accessibility of the lattice ground state during demagnetization, which subsequently results in a reduction of ΔE^* for $\Psi_{0.02}$ compared to $\Psi_{0.16}$. Short-range magnetic charge ordering occurs in the global ground states for $\Psi_{0.16}$ and $\Psi_{0.02}$. The biggest difference in behavior takes place between Motif 1–4 pairs. In $\Psi_{0.16}$ the Motif 1–4 pairs occur along the structural domain boundaries and have adjacent magnetic charges with the same sign. By comparison, the Motif 1–4 pairs of $\Psi_{0.02}$ have both alternating and same-sign magnetic charge. Another aspect of the Motif 1–4 pairs is the formation of degenerate spins on their shared island, for which the lack of a preferred spin orientation results in a local energy minimum.

A two-fold globally degenerate ground state of antiferromagnetic-aligned motifs was simulated for the Ψ_1 and $\Psi_{0.22}$ geometries, replicating the ordering of the square ASI ground state. The same behavior was seen for the $\Psi_{0.16}$ lattice (Fig. 5a), with the exception that the simulated ground state contains a single higher energy motif that sits on the 3-fold symmetry axis. An unexpected result was that this behavior extended to the ground state simulated for the disordered $\Psi_{0.02}$ lattice as well. While the majority of spins collectively participate in one of two distinct global spin arrangements (see the black spins of Fig. 5b), a disperse set of randomly-arranged degenerate spins also remain in the ground state (white spins of Fig. 5b). Vertex frustration prohibits all motifs from occupying the E0 energy state, leading to some higher energy motif excitations being "frozen-in". This behavior has also been observed in other periodic and aperiodic ASIs.[7,8] However, the spatial distribution of frozen excitations and degenerate spins is highly dependent on the lattice geometry and determining the true ground state for a disordered lattice is non-trivial.

After analysing the demagnetized state and ground state of the RASI lattices, we see that the long-range magnetization behavior is more effectively described by the motif populations (see Fig. 4c) than by the characteristic order parameter Ψ. While Ψ characterizes the *global* ordering, the behavior that we have observed depends on the *local* magnetic interactions. This explains why the magnetization behavior does not change monotonically with Ψ; instead, similar behavior is observed between lattices with comparable local ordering. Finally, we

have observed two factors that can increase the accessibility of the ground state in RASIs: (1) increasing the population of motifs with a highly degenerate, low-energy configuration and (2) increasing the length and number of unfrustrated chains of strongly-coupled islands, which favor head-to-tail order. Further investigation of RASIs with increased motif degeneracy and island chain frustration may lead to disordered RASI lattices with degenerate but well-described behavior. This can have implications for designer magnetic charge propagation and provide insights into controlling the behavior of artificial spin glass systems.

Conclusion

We have demonstrated the significance of geometry and lattice symmetry on the magnetic domain behavior in rhombus artificial spin ices, by systematically varying the lattice order. The demagnetized Ψ_1 RASI had the lowest energy difference from its ground state and exhibited anisotropic domain behavior stemming from the rotational symmetry of both the lattice and the motif geometry that enables chains of strongly coupled nanomagnets. $\Psi_{0.22}$ and $\Psi_{0.16}$ showed a similar behavior, albeit on a smaller scale, with shorter, frustrated chains of aligned nanomagnets forming smaller magnetic domains and more motifs in excited states forming domain walls. Similar behavior was seen in the disordered $\Psi_{0.02}$ RASI, but $\Psi_{0.02}$ had reduced lattice energy due to a larger population of motifs with large configurational degeneracy. Finally, we observed that rotational demagnetization slightly lowered the net magnetization of the lattices but was more effective at lowering the energy closer to the simulated ground state of the Ψ_1 and $\Psi_{0.02}$ RASIs compared to that of the $\Psi_{0.22}$ and $\Psi_{0.16}$ lattices. A comparative analysis of the motif energy and motif ordering in each lattice allowed us to achieve a greater understanding of the magnetic domain behavior as a function of lattice geometry, but more work is needed to understand the global collective behavior in the order-disorder transition of RASIs.

It would be of great interest to further understand the interplay of island chains and degenerate Type 1 motifs as a means to characterize both a lattice and its behavior. For instance, while Ψ_1 has highly anisotropic magnetic charge propagation, a study of the "dice"[32] lattice (which is equivalent to Ψ_{-1}), showed magnetic charge screening behavior. Thus, it may be possible to create lattices of mixed character to control mobile pathways and pinning sites for magnetic charge propagation. Additionally, understanding the effects of quenched disorder and magnetic frustration for the development of artificial spin glasses is still a growing subfield of ASI research.[16]

Experimental

Experimental methods

Four rhombus artificial spin ice (RASI) lattices were patterned utilizing focused electron beam-induced deposition (FEBID) onto Si_3N_4 TEM windows using a FIB FEI Nova 600 Nanolab. A ~1 nm underlayer of carbon was deposited across the whole membrane to reduce charging during TEM imaging. The incident electron beam voltage for deposition was 5 kV with a current of 1.1 nA. A single pass of the electron beam patterned the lattices while $Co_2(CO)8$ flowed from a gas injection source, with a base pressure of 2×10^{-6} Torr and a working pressure of 1×10^{-5} Torr. A 1 nm capping layer of C was deposited over the entire sample to reduce oxidation, and a 3 nm cap layer of Al was then deposited using e-beam evaporation to prevent longer term degradation. The dimensions of each magnetic island were approximately 200 nm $\times$ 50 nm, with a 10 nm thickness. The vertex-to-vertex spacing was 300 nm.

The prefactors of the Ψ equation, which define the ideal random lattice as $\Psi = 0$, were discussed in Stannard *et al*.[33] The authors utilized continuous-time Monte Carlo (MC) simulations of rhombus mixing on a lattice in which neighboring tiles with rotational symmetry or mirror symmetry were modeled to have equivalent tiling energy ($\varepsilon_r = \varepsilon_m$). The output of the simulations results in a tiling that maximizes the configurational entropy and is therefore an ideal random tiling. By averaging the relative populations of tile pairs with rotational symmetry or mirror symmetry present over numerous MC runs, the prefactors can be calculated, which results in the equation for Ψ.

Reconstructed magnetic induction maps of the RASIs were created using LTEM images acquired in a JEOL 2100F aberration-corrected Lorentz transmission electron microscope. Two through-focal-series (TFS) in reference and 180°-flipped orientations were used for magnetic phase retrieval. The TFS had a quadratic defocus step with seven steps total (i.e. 1 µm, 4 µm, 9 µm …, 49 µm) for a total of 15 bright-field images (1 in-focus, 7 under-focused, 7 over-focused) of the sample in a field-free region of the microscope. Magnetic phase retrieval was performed by solving the transport of intensity equation using an open-source Python package developed by our group[41]. The magnetization direction of individual islands is determined by comparing the color of the island in the magnetic induction map to the accompanying color-wheel. The magnetization is parallel to the direction pointing from the center of the color-wheel to the matching island color on the edge of the color-wheel.

Rotational demagnetization was performed by rotating the sample in a decreasing magnetic field. The TEM grid was positioned between the poles of an electromagnet and the rotation was controlled with a stepper motor. The rate of rotation was 1,000 rpm and the magnetic field was in the sample plane. An initial saturating field of 1,000 G was applied and reduced linearly at a rate of 3.5 G/s until a field of 0 G was obtained.

Simulation details

Micromagnetic simulations were performed using the MuMax3 software[34] to determine the energy of all possible magnetic configurations of the RASI vertex motifs. The discretized grid consisted of cells with dimensions of 2.5 nm x 2.5 nm x 10 nm. Modeling parameters for Co included a saturation magnetization of 1.42×10^6 A/m and exchange stiffness constant of 2.50×10^{-11} J/m.[42] The magnetization of each cell in

an individual island was pre-set along the long axis of the island according to the unique magnetic configuration of its vertex motif, followed by a relaxation to lower the magnetostatic energy.

Author Contributions

T. C.: Conceptualization, formal analysis, investigation, methodology, validation, visualization, writing – original draft, writing – review & editing. A. K. P. L.: Conceptualization, funding acquisition, project administration, writing – review & editing. C. P.: Conceptualization, methodology, funding acquisition, project administration, writing – review & editing, supervision. All authors have read and agreed to the submitted version of the manuscript.

Data availability

The data that supports the findings of this study are available upon reasonable request from the corresponding author (cd@anl.gov).

Conflicts of interest

There are no conflicts to declare.

Acknowledgements

This work was funded by the US Department of Energy, Office of Science, Office of Basic Energy Sciences, Materials Science and Engineering Division. Work performed at the Center for Nanoscale Materials, a U.S. Department of Energy Office of Science User Facility, was supported by the U.S. DOE, Office of Basic Energy Sciences, under Contract No. DE-AC02-06CH11357.

Notes and references

‡ Electronic supplementary information (ESI) available. See DOI:

References

1 P. A. M. Dirac, *Proc Roy Soc Lond A*, 1931, **133**, 60–72.
2 C. Castelnovo, R. Moessner and S. L. Sondhi, *Nature*, 2008, **451**, 42–45.
3 S. Ladak, D. E. Read, G. K. Perkins, L. F. Cohen and W. R. Branford, *Nat. Phys.*, 2010, **6**, 359–363.
4 J. P. Morgan, A. Stein, S. Langridge and C. H. Marrows, *Nat. Phys.*, 2011, **7**, 75–79.
5 R. F. Wang, C. Nisoli, R. S. Freitas, J. Li, W. McConville, B. J. Cooley, M. S. Lund, N. Samarth, C. Leighton, V. H. Crespi and P. Schiffer, *Nature*, 2006, **439**, 303–306.
6 S. Zhang, I. Gilbert, C. Nisoli, G. W. Chern, M. J. Erickson, L. O'Brien, C. Leighton, P. E. Lammert, V. H. Crespi and P. Schiffer, *Nature*, 2013, **500**, 553–557.
7 C. Nisoli, V. Kapaklis and P. Schiffer, *Nat. Phys.*, 2017, **13**, 200–203.
8 M. J. Morrison, T. R. Nelson and C. Nisoli, *New J. Phys.*, , DOI:10.1088/1367-2630/15/4/045009.
9 N. Rougemaille and B. Canals, *Eur. Phys. J. B*, , DOI:10.1140/epjb/e2018-90346-7.
10 W. R. Branford, S. Ladak, D. E. Read, K. Zeissler and L. F. Cohen, *Science*, 2012, **335**, 1597–1600.
11 H. Arava, N. Leo, D. Schildknecht, J. Cui, J. Vijayakumar, P. M. Derlet, A. Kleibert and L. J. Heyderman, *Phys. Rev. Appl.*, 2019, **11**, 1–6.
12 J. C. Gartside, K. D. Stenning, A. Vanstone, H. H. Holder, D. M. Arroo, T. Dion, F. Caravelli, H. Kurebayashi and W. R. Branford, *Nat. Nanotechnol.*, 2022, **17**, 460–469.
13 I. Gilbert, Y. Lao, I. Carrasquillo, L. O'brien, J. D. Watts, M. Manno, C. Leighton, A. Scholl, C. Nisoli and P. Schiffer, *Nat. Phys.*, 2016, **12**, 162–165.
14 Y. Lao, F. Caravelli, M. Sheikh, J. Sklenar, D. Gardeazabal, J. D. Watts, A. M. Albrecht, A. Scholl, K. Dahmen, C. Nisoli and P. Schiffer, *Nat. Phys.*, 2018, **14**, 723–727.
15 X. Zhang, A. Duzgun, Y. Lao, S. Subzwari, N. S. Bingham, J. Sklenar, H. Saglam, J. Ramberger, J. T. Batley, J. D. Watts, D. Bromley, R. V. Chopdekar, L. O'Brien, C. Leighton, C. Nisoli and P. Schiffer, *Nat. Commun.*, 2021, **12**, 4–10.
16 M. Saccone, F. Caravelli, K. Hofhuis, S. Parchenko, Y. A. Birkhölzer, S. Dhuey, A. Kleibert, S. van Dijken, C. Nisoli and A. Farhan, *Nat. Phys.*, 2022, **18**, 517–521.
17 V. Brajuskovic, A. Addi, C. Phatak and A. K. Petford-Long, *Phys. Rev. B*, 2018, **98**, 94424.
18 A. May, M. Hunt, A. Van Den Berg, A. Hejazi and S. Ladak, *Commun. Phys.*, 2019, **2**, 13.
19 R. Cheenikundil, J. Bauer, M. Goharyan, M. d'Aquino and R. Hertel, *APL Mater.*, 2022, **10**, 081106.
20 Y. Perrin, B. Canals and N. Rougemaille, *Nature*, 2016, **540**, 410–413.
21 A. Farhan, M. Saccone, C. F. Petersen, S. Dhuey, R. V. Chopdekar, Y.-L. Huang, N. Kent, Z. Chen, M. J. Alava, T. Lippert, A. Scholl and S. van Dijken, *Sci. Adv.*, 2019, **5**, eaav6380.
22 F. Barrows, V. Brajuskovic, A. K. Petford-Long and C. Phatak, *Phys Rev B*, 2019, **99**, 94424.
23 B. Farmer, V. S. Bhat, J. Sklenar, J. Woods, E. Teipel, N. Smith, J. B. Ketterson, J. T. Hastings and L. E. De Long, *J. Appl. Phys.*, 2014, **115**, 3–6.
24 A. Frotanpour, J. Woods, B. Farmer, A. P. Kaphle, L. E. De Long, L. Giovannini and F. Montoncello, *Phys. Rev. B*, 2020, **102**, 224435.
25 J. Drisko, T. Marsh and J. Cumings, *Nat. Commun.*, 2017, **8**, 1–8.
26 Z. Budrikis, P. Politi and R. L. Stamps, *J. Appl. Phys.*, 2012, **111**, 109–112.
27 A. Frotanpour, J. Woods, B. Farmer, A. P. Kaphle, J. T. Hastings and L. E. DeLong, *Phys Rev B*, 2021, **103**, 184402.
28 M. Saccone, K. Hofhuis, D. Bracher, A. Kleibert, S. Van Dijken and A. Farhan, *Nanoscale*, 2020, **12**, 189–194.
29 I. Recio and J. J. Torres, *Neural Netw.*, 2016, **84**, 91–101.
30 M. Saccone, A. Scholl, S. Velten, S. Dhuey, K. Hofhuis, C. Wuth, Y. L. Huang, Z. Chen, R. V. Chopdekar and A. Farhan, *Phys. Rev. B*, 2019, **99**, 1–7.
31 Y. Shi, C. Nisoli and G.-W. Chern, *Appl. Phys. Lett.*, 2021, **118**, 122407.
32 A. Farhan, A. Scholl, C. F. Petersen, L. Anghinolfi, C. Wuth, S. Dhuey, R. V. Chopdekar, P. Mellado, M. J. Alava and S. Van Dijken, *Nat. Commun.*, 2016, **7**, 8–13.

33 A. Stannard, J. C. Russell, M. O. Blunt, C. Salesiotis, M. D. C. Giménez-López, N. Taleb, M. Schröder, N. R. Champness, J. P. Garrahan and P. H. Beton, *Nat. Chem.*, 2012, **4**, 112–117.
34 A. Vansteenkiste, J. Leliaert, M. Dvornik, M. Helsen, F. Garcia-Sanchez and B. Van Waeyenberge, *AIP Adv.*, , DOI:10.1063/1.4899186.
35 J. D. Bernal and R. H. Fowler, *J. Chem. Phys.*, 1933, **1**, 515–548.
36 V. Brajuskovic, F. Barrows, C. Phatak and A. K. Petford-Long, *Sci. Rep.*, 2016, **6**, 1–10.
37 C. Phatak, A. K. Petford-Long, O. Heinonen, M. Tanase and M. De Graef, *Phys. Rev. B - Condens. Matter Mater. Phys.*, , DOI:10.1103/PhysRevB.83.174431.
38 X. Ke, J. Li, C. Nisoli, P. E. Lammert, W. McConville, R. F. Wang, V. H. Crespi and P. Schiffer, *Phys. Rev. Lett.*, 2008, **101**, 18–21.
39 S. A. Morley, J. M. Porro, A. Hrabec, M. C. Rosamond, D. A. Venero, E. H. Linfield, G. Burnell, M.-Y. Im, P. Fischer, S. Langridge and C. H. Marrows, *Sci. Rep.*, 2019, **9**, 15989.
40 Y. Nambu, *Phys. Rev. D*, 1974, **10**, 4262–4268.
41 A. R. C. McCray, T. Cote, Y. Li, A. K. Petford-Long and C. Phatak, *Phys. Rev. Appl.*, , DOI:10.1103/PhysRevApplied.15.044025.
42 Y. Guerra, R. Peña-Garcia and E. Padrón-Hernández, *J. Magn. Magn. Mater.*, 2018, **452**, 17–22.